Journal of Materials Science & Technology 133 (2023) 238–248

Contents lists available at ScienceDirect

Journal of Materials Science & Technology

journal homepage: www.elsevier.com/locate/jmst

Research Article

Hierarchical graphene@MXene composite foam modified with flower-shaped FeS for efficient and broadband electromagnetic absorption

Shuangshuang Li, Xinwei Tang, Xu Zhao, Shijie Lu, Jiangtao Luo, Zheyuan Chai, Tiantian Ma, Qianqian Lan, Piming Ma, Weifu Dong, Zicheng Wang*, Tianxi Liu*

The Key Laboratory of Synthetic and Biological Colloids, Ministry of Education, School of Chemical and Material Engineering, International Joint Research Laboratory for Nano Energy Composites, Jiangnan University, Wuxi 214122, China

ARTICLE INFO

Article history:
Received 29 April 2022
Revised 3 June 2022
Accepted 10 June 2022
Available online 9 July 2022

Keywords:
Graphene
MXene
Iron sulfide
Hierarchical structure
Foam
Microwave absorption

ABSTRACT

Developing high-performance broadband microwave absorption material becomes an urgent concern in the field of electromagnetic protection. In this work, an ultralight magnetic composite foam was constructed by electrostatic self-assembly of MXene on the surface of graphene skeletons, and subsequent hydrothermal anchoring of flower-shaped FeS clusters. Under the synergistic effect of MXene coating increasing conductive loss and FeS clusters improving magnetic loss, the rational construction of hierarchical impedance structure in foam can effectively promote the entrance and consumption of more incident electromagnetic waves. The minimum reflection loss (RL_{min}) reaches –47.17 dB at a thickness of 4.78 mm, and the corresponding effective absorption bandwidth (EAB) is up to 6.15 GHz. More importantly, the microwave absorption performance of composite foam can be further optimized by controlling the loading of MXene and thermal treatment at a low temperature. The maximum of EAB for GMF-300 can be extended to an unprecedented value of 11.20 GHz (covering 6.10–17.30 GHz).

1. Introduction

Designing and assembling high-performance microwave absorption (MA) material becomes an urgent concern in the field of electromagnetic protection [1–4]. Up to now, carbon-based materials as an alternative candidate to ponderous and erodible ferrites, ceramics, and their hybrids, have been successfully prepared and exhibit comparable MA performance [5–12]. Among these carbon materials, graphene-based porous material (foam or aerogel) attracts increasing interest and displays a unique competitive advantage in MA performance due to the enhanced multiple reflection/scattering loss between internal surfaces of three-dimensional (3D) skeletons [13–15].

In literature, many graphene-based foam/aerogels are fabricated through self-assembly between graphene oxide (GO) nanosheets and followed by annealing treatment [16–19], or compositing with high-conductive fillers [20,21]. On the one hand, the annealing treatment is considered as an efficient route to promote the improvement in electrical conductivity of the foams. However, the higher-temperature annealing treatment (> 500 °C) for a long time leads to the degradation in mechanical properties of composite foams and enormous energy consumption. For example, Gao et al. [19] successfully prepared ordered lamellar graphene aerogel via a directional freezing method and carbonization at 2500 °C. The sample reveals an outstanding electromagnetic interference shielding value of ~65 dB, but the weak mechanical properties needed to be improved by encapsulating polydimethylsiloxane (PDMS) resin into the aerogel. On the other hand, the effective composite of conductive fillers with reduced graphene oxide (rGO) nanosheets can solve the above defects and endow the foams with excellent MA performances [20,21]. As reported by Lv et al. [20], carbon nanotube/ graphene aerogel (CNTs/GA) was prepared via a simple hydrothermal and freeze-drying route. The obtained sample exhibits a high RL_{min} value of –31.0 dB, and a broad EAB from 18 to 26.5 GHz. However, the formation of the conductive network in foam mainly relies on the synergistic composite effect between rGO nanosheets and high-conductive fillers. As a result, the isolation of rGO with low conductivity hinders the formation of a higher conductive path in porous network, seriously restricting the electromagnetic energy dissipation as a conductive loss.

---

* Corresponding authors.
E-mail addresses: wangzc@jiangnan.edu.cn (Z. Wang), txliu@jiangnan.edu.cn (T. Liu).

https://doi.org/10.1016/j.jmst.2022.06.018

In recent years, many explorations are attempted to directly load the conductive coating on the surface of rGO skeletons [22,23]. As reported by Wang et al. [22], high-conductive polyaniline coating is covalently bonded on the surface of reduced graphene oxide aerogel (PANI/GA) via using hydrothermal (95 °C) and *in-situ* polymerization techniques. The obtained PANI/GA shows a comparable RL_{min} of –42.3 dB, and the corresponding EAB covers 3.2 GHz. However, most incident electromagnetic waves (EMW) would be reflected, owing to the generation of impedance mismatching between conductive coating and air. Hence, it is necessary to introduce a dielectric coating to further optimize the impedance distribution of porous skeletons. For example, Wang et al. [24] introduced MXene on the surface of carbon fiber by self-assembly and then loaded a layer of dielectric MoS_2 by hydrothermal reaction. The MA performance of compact composite can be regulated and optimized: the optimal RL_{min} reaches –61.51 dB and the maximum EAB achieves 7.6 GHz.

In addition, to improve the impedance matching and attenuation characteristic of incident EMW, many efforts are devoted to introducing magnetic materials on the surface of conductive coating [25,26]. For example, Fang et al. [25] prepared rGO/Cu/Fe_3O_4 composite through a one-step hydrothermal method. The RL_{min} reaches a low value of –40 dB and the maximum EAB can be extended to a broader value of 5.2 GHz. In those systems, the absorption mechanism of these magnetic particles mentioned above only depends on their isotropic magnetic loss. Recently, many literatures confirm that the microstructure of magnetic particles plays an important role in the efficient consumption of EMW [27,28]. For instance, Ma et al. [27] developed a flower-shaped Co_3O_4/rGO hybrid. The formation of flower-shaped Co_3O_4 clusters acted as microwave scattering sites, promoting the generation of more multiple reflection/ scattering. As a result, the hybrids present an optimal RL_{min} of –61 dB. Therefore, the construction of magnetic graphene-based composite foam with a hierarchical impedance structure becomes the key challenge for preparing high-performance microwave absorbing materials. However, to date, how to realize the effective loading of conductive coating and anisotropic magnetic clusters on rGO foam is rarely reported.

In this work, we report a simple and effective approach to fabricating magnetic composite foam by electrostatic self-assembly of MXene on the surface of rGO skeletons and subsequent hydrothermal anchoring of flower-shaped FeS clusters. The loading of MXene coating increasing conductive loss and FeS clusters improving magnetic loss on the surface of rGO skeletons promotes the formation of hierarchical impedance structure in foams. As a consequence, the effective construction of the hierarchical impedance structure can accelerate the entry of more incident EMW. Under the synergistic effects of various magnetic loss, interfacial polarization, conductive loss, and multiple reflections/scattering, the formation of the multi-hierarchical structure further enhances the attenuation characteristic for EMW entering the foam. More importantly, the adjustment in the loading of MXene and thermal treatment at a low temperature can become an effective means to realize the optimization of whole impedance distribution, endowing the foam with an outstanding absorption capacity and bandwidth.

2. Experimental

2.1. Materials

The GO was synthesized by an improved Hummers' method [29,30]. Ethanediamine (EDA), Ferrous sulfate heptahydrate ($FeSO_4·7H_2O$, Analytical grade), and ethanol were purchased from Sinopharm Chemical Reagent Co., Ltd. *L*-cysteine (99%) and Polyethyleneimine (PEI, 50% in water) were purchased from Damas-beta and Innochem, respectively.

2.2. Preparation of rGO foam

GO powder was added into deionized water (4 mg/mL) and vigorously stirred with sonication for 30 min. As a cross-linking agent, EDA (100 mg) was subsequently added to GO suspension as a cross-linking agent. After vigorously stirring, the homogeneous suspension was sealed in sample bottles and hydrothermally treated at 80 °C for 24 h without stirring. After that, the obtained hydrogel was dialyzed with deionized water to remove residual EDA, avoiding excessive shrinkage in volume. For foam preparation, the hydrogel was freeze-dried to remove the remaining water inside. In the hydrothermal process, EDA can be used as the reducing agent for partly removing the hydroxyl, carboxyl, and epoxy groups of GO nanosheets. Hence, the product was named as rGO foam.

2.3. Preparation of GN/MXene/FeS foam

rGO/MXene/FeS foam was fabricated via a two-step process. Firstly, 0.5 mL PEI was dissolved into 20 mL deionized water. The above rGO foam was impregnated into PEI solution for 24 h. Afterward, the residual PEI was removed by multiple dialysis with deionized water. And then, the foam was vacuum-impregnated in 30 mg/mL MXene dispersions in the same way. After the dialyzing and freeze-drying processes, rGO/MXene composite foam was obtained. Secondly, 0.70 g $FeSO_4·7H_2O$ and 0.30 g *L*-cysteine were separately dissolved in 10 mL water to obtain two solutions. And then, they were mixed and violently stirred for 20 min. The as-prepared rGO/MXene was subsequently dipped in the mixed solution. The mixture was seated in a Teflon-lined stainless-steel autoclave and maintained at 200 °C for 24 h. Then, the obtained product was washed with deionized water, and freeze-drying. The obtained sample was labeled as rGO/MXene/FeS foam (rGMF as a reference without special emphasis). As control, the loading concentrations of MXene were adjusted to the value of 10, 20, 30, and 40 mg/mL, which were marked as rGMF-10, rGMF-20, rGMF-30 (rGMF), and rGMF-40, respectively. In addition, the rGO/MXene/FeS foams were heat-treated at 200, 300, and 400 °C under an N_2 atmosphere. The corresponding samples (GN/MXene/FeS) were denoted as GMF-200, GMF-300 and GMF-400, respectively. The preparation process of GN/MXene/FeS composite foam was described in Fig. 1(a).

2.4. Characterizations

Scanning electron microscopy (SEM) was measured on a Hitachi S-4800 field-emission scanning electron microscope at an accelerating voltage of 30 kV. X-ray diffraction (XRD) patterns were characterized on a Bruker D8 X-ray diffractometer with a Cu $K\alpha$ X-ray source (λ = 1.5418 Å). The magnetic properties were recorded by a magnetic property measurement system (SQUID-VSM) at 300 K. The electromagnetic parameters were measured on a vector network analyzer (Agilent 8720ET) in the frequency range of 0.5–18.0 GHz. The testing foams were immobilized by encapsulating paraffin as a supporting matrix. The mixture was made into toroidal-shaped samples with an outer diameter of 7.0 mm, an inner diameter of 3.0 mm, and a thickness of 2–4 mm. The percentage of paraffin in the samples was ~85 wt.%.

3. Results and discussion

3.1. Structure and morphology of composite foams

The fabrication of GN/MXene/FeS composite foam is illustrated in Fig. 1(a). Firstly, rGO foam was prepared by a mild hydrothermal reaction between GO and EDA, and a freeze-drying process [18,31]. It is worthy to note that EDA plays a crucial role in accelerating the

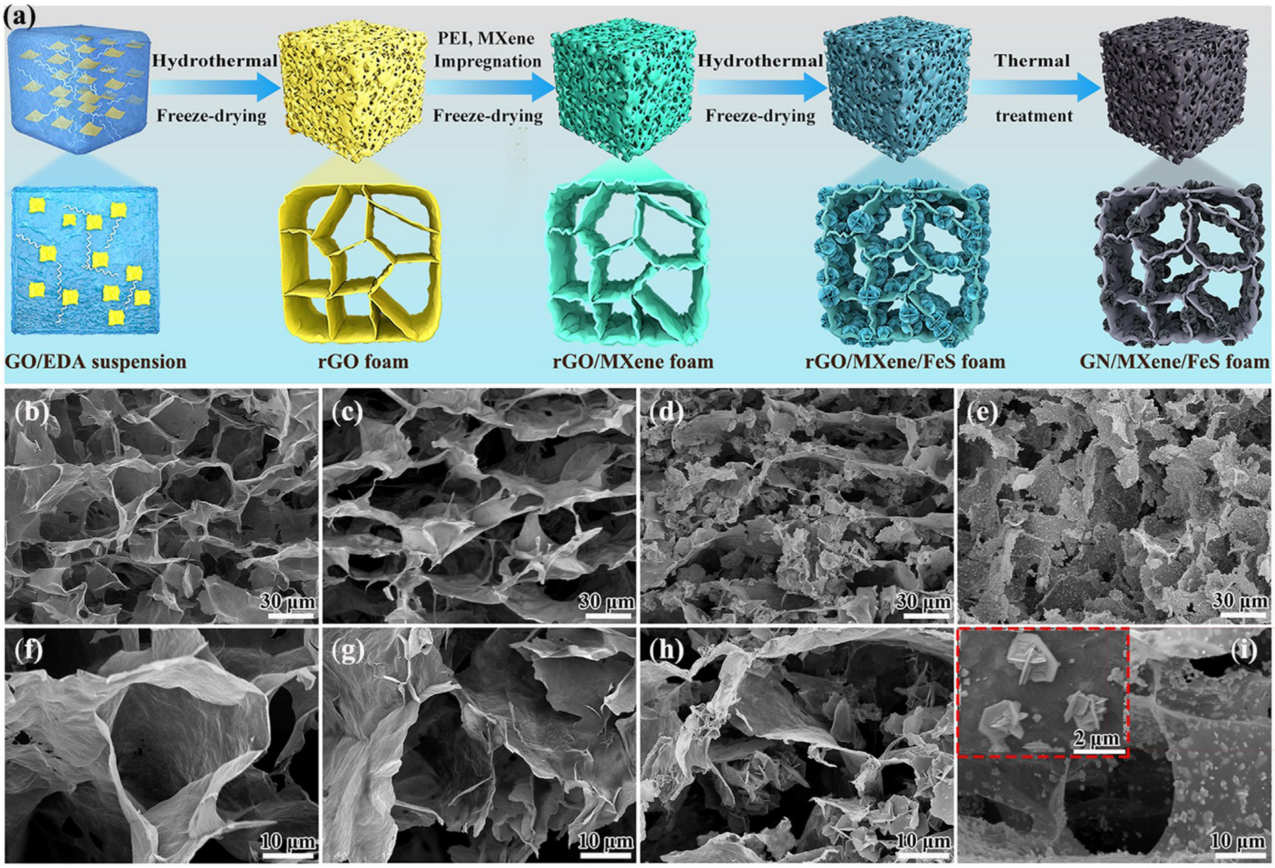

Fig. 1. (a) Preparation process of GN/MXene/FeS foam; SEM images of those foams: (b, f) rGO; (c, g) rGO/MXene; (d, h) rGO/MXene/FeS; (e, i) GN/MXene/FeS (The small picture embedded in the upper left corner is a partial magnification of 5000 times).

formation of isotropous 3D network structure through crosslinking reaction between the epoxy groups of GO and amino groups in EDA. As shown in Fig. 1(b, f), a cross-linked porous network with a smooth inner surface is successfully constructed in rGO foam. Besides, it is worthy to note that the large aspect ratio of graphene nanosheets endows the rGO foam with excellent flexibility in comparison with rigid MXene. The flexible matrix further provides enough support to load MXene coating and FeS clusters. Secondly, for achieving the effective loading of conductive coating, rGO foam is positively charged by PEI modification and then immersed in MXene suspension. Owing to the existence of abundant functional groups (–OH, –O, –F), the negative MXene nanosheets can be electrostatically adsorbed on the inner surface of PEI-modified rGO foam. As displayed in Fig. 1(c, g), the surface of rGO foam becomes rough. Meanwhile, it can be distinctly observed that many small flakes are tightly attached to the rGO skeletons, which may be assigned to the MXene nanosheets. As a control, the samples were also characterized by XRD, XPS, and VSM. As shown in Fig. 2(a), a new X-ray diffraction peak of 6.68° appears in rGO/MXene foam apart from the characteristic peak of rGO around 24.5°. It agrees well with that of pure MXene [32]. Additionally, A similar phenomenon arises in the XPS spectra. In comparison with rGO foam, the XPS spectrum of rGO/MXene foam exhibits two new binding peaks centered at ~680 and ~452 eV (Fig. 2(b)), corresponding to *F* 1s and Ti 2p3, respectively [33]. Those results once again confirm the successful loading of MXene on the surface of rGO foam.

Thirdly, for improving the impedance matching and attenuation characteristic of foams, the magnetic FeS clusters are needed to grow on the surface of rGO/MXene by hydrothermal reaction. As a precursor, *L*-cysteine has a strong tendency to coordinate with inorganic cations, owing to the existence of –NH_2, –COOH, and –SH functional groups. In this system, *L*-cysteine reacts with Fe^{2+} to form a relatively stable Fe-cysteine complex. And then, the complex decomposes to form FeS particles under the following hydrothermal condition (200 °C and 24 h). During the hydrothermal process, those primary particles aggregate together, nucleate, crystallize, and grow. Subsequently, as the reaction proceeds, these initial FeS nuclei form nanopetals based on the precipitation solubility equilibrium in the solution [34,35]. Under the influence of the magnetic dipole–dipole interactions and the anisotropic magnetic forces, the new nanopetals in the solution tended to join with each other to reduce both magnetic anisotropic energy and surface energy. Finally, quasi-spherical petal-built aggregates with rugged surfaces are formed. As depicted in Fig. 1(d, h), many flower-shaped clusters are dispersed on the surface of rGO/MXene. As characterized by XRD, the appearance of those peaks at 30.0°, 33.9°, 44.8°, 53.3°, and 71.6° (Fig. 2(a)) confirms the formation of FeS hybrids in rGMF foam, corresponding to (200), (203), (206), (220), and (406) indexed planes of Fe_7S_8 (PDF#29-0723) [36,37]. Meanwhile, the new binding peaks of Fe 2p (710.7 eV), S 2s (203.7 eV), and S 2p (168.7 eV) arise in rGMF foam, which once again suggests the formation of Fe_7S_8 [34,35]. Moreover, as shown in Fig. 2(c), the as-prepared foam exhibits obvious saturation magnetization (*Ms*) of 2.1 emu/g and coercivity (*Hc*) of 557.18 Oe, while that of rGO and rGO/MXene foam is close to 0. Based on the above-mentioned discussion, we can conclude that the magnetic rGO/MXene/FeS composite foam with a hierarchical structure is successfully constructed.

Finally, to further optimize the impedance distribution of the foams, a series of thermal treatments (200–400 °C) can be car-

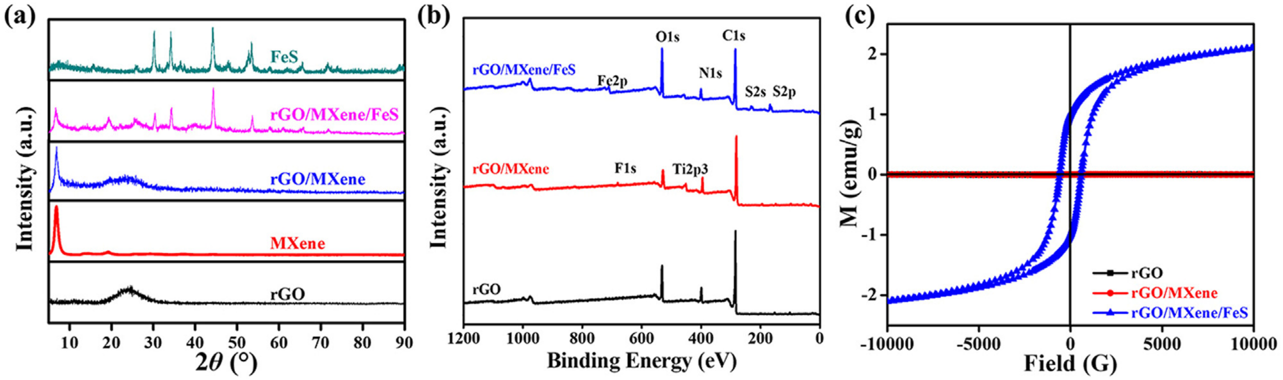

Fig. 2. (a) XRD patterns of FeS, rGO, MXene, rGO/MXene, and rGO/MXene/FeS; (b) XPS spectra and (c) hysteresis loops of rGO, rGO/MXene, and rGO/MXene/FeS foam.

ried out as displayed in Fig. 1(a). After annealing treatment at 400 °C, a similar flower-shaped micro-morphology with partial volume shrinkage can be still observed in the obtained foam, as shown in Fig. 1(e,i). The volume shrinkage does not destroy the 3D architecture of flower-shaped FeS clusters, which is crucial to the multiple reflection/scattering of incident EMW. Furthermore, the result of XRD suggests that the crystal structure of FeS hybrids can be retained after heating treatment (Fig. S1 in the Supplementary Material). In the middle layer, the MXene nanosheets have been proved to possess excellent thermal stability and electrical conductivity after heating treatment (< 400 °C) in an inert atmosphere [38]. Additionally, the residual functional groups of innermost rGO skeletons can be easily thermally removed, thereby facilitating the restoration of the electrical conductivity of graphene sheets. Based on the above, the thermal treatment at relative-low temperature makes it possible to modulate impedance matching and attenuation characteristics in the hierarchical composite foams.

3.2. Electromagnetic parameters of composite foams

To investigate the microwave absorption performance of the composite foam, the complex permittivity ($\varepsilon_r = \varepsilon' - j\varepsilon''$) and permeability ($\mu_r = \mu' - j\mu''$) were measured on a vector network analyzer. The electromagnetic parameters are calculated and displayed in Figs. 3 and 4. As shown in Fig. 3(a–c), the complex permittivity (ε' and ε'') and dielectric loss tangent ($\tan\delta_\varepsilon = \varepsilon''/\varepsilon'$) exhibit a general tendency to increase with the effective construction of hierarchical foams. Compared with rGO foam, the improvement in rGO/MXene foam can be attributed to the successful loading of highly conductive MXene sheets on the surface of rGO skeletons. For rGO/MXene/FeS foam, the further enhancement in permittivity properties may be ascribed to the hydrothermal reduction of rGO skeletons, the introduction of FeS hybrids, and the corresponding air-extrusion effect. Besides, it is worth noting that a resonance peak for rGO/MXene/FeS foam arises at 8–15 GHz. To identify the factors devoting to the permittivity properties, the plots of ε'' versus ε' are displayed in Fig. 3(d–f). As to rGO foam, several small semicircles appear in Fig. 3(d), suggesting different Debye relaxation processes. It might be due to the dipole polarization of plentiful residual functional groups and/or defects in rGO foam [39]. After being incorporated with MXene coating, the plot of rGO/MXene foam exhibits two obvious Cole–Cole semicircles with a bigger diameter. It may be caused by the interfacial polarization between rGO skeleton and MXene coating (as shown in Fig. 5(a)) [40], and the dipole polarization of rGO foam as mentioned above, respectively. Besides, a line tail arises in rGO/MXene curve, which can be regarded as the conductive loss originating from the high-conductive MXene coating (as displayed in Fig. 5(d)) [41–43]. It indirectly confirms that MXene is successfully loaded on the rGO skeletons. After loading of FeS hybrids, the plot of rGO/MXene/FeS shows a dramatic evolution distinguished from the above foams (Fig. 3(f)). There are two semicircles and a line tail extended to a higher position, revealing the progressive improvement in dielectric loss and conductive loss. Those relaxation processes may correspond to the interfacial polarization of rGO/MXene and MXene/FeS (Fig. 5(a)), and stronger conductive loss originated from MXene and hydrothermal reduced rGO (Fig. 5(d)), respectively.

On the other hand, the complex permeability of the corresponding foams displays a similar tendency to increase with the effective construction of the hierarchical structure as shown in Fig. 4(a, b). As to rGO/MXene/FeS, the magnetic loss tangent curve exhibits two resonance peaks at 8–11.5 GHZ and 11.5–18 GHz, which is higher than that of rGO and rGO/MXene foam (Fig. 4(c)). It verifies the successful introduction of magnetic FeS hybrids. As to magnetic loss, the loss form mainly includes magnetic hysteresis, domain wall resonance, eddy current loss, natural resonance, and exchanged resonance. The magnetic hysteresis and domain wall resonance may be easily excluded because of the mismatch of applied field and frequency [43]. To judge the existence of eddy current loss, C_0 can be evaluated according to Eq. (1):

$$C_0 = \mu''\left(\mu'\right)^{-2}(f)^{-1} = 2\pi\mu_0 d^2\sigma/3 \qquad (1)$$

where μ_0 and σ are the permeability of the vacuum and the electrical conductivity, respectively. In general, if C_0 is a constant with the change of frequency, it indicates that only eddy current loss exists in the absorber. If not, there are other magnetic losses in the system. As shown in Fig. 4(d), it can be clearly observed that the C_0 value of the foams exhibits gradually increased fluctuation as MXene and FeS hybrids are sequentially loaded on rGO skeletons. It indicates that for rGO/MXene/FeS foam, the natural resonance and exchanged resonance also play an indispensable role in magnetic dissipation apart from eddy current loss (as demonstrated in Fig. 5(e)). Additionally, it can be found that the value of dielectric loss tangent is higher than that of magnetic loss tangent at the frequency range of 0.5–13.5 GHz, while they reverse at 13.5–18 GHz. Therefore, it can be concluded that the dielectric loss plays a dominant role in electromagnetic energy consumption rather than the magnetic loss at low- and mid-frequency, whereas the magnetic loss covers the energy loss at high-frequency.

Based on those electromagnetic parameters, the equivalent characteristic impedance ($Z = |Z_{in}/Z_0|$) can be calculated to estimate the impedance matching of the foams according to Eq. (2):

$$Z_{in} = Z_0\sqrt{\frac{\mu_r}{\varepsilon_r}}\tanh\left[j\left(\frac{2\pi fd}{c}\right)\sqrt{\mu_r\varepsilon_r}\right] \qquad (2)$$

where Z_{in} and Z_0 are the impedance of samples and vacuum; μ_r and ε_r are the relative permeability and permittivity; d is the thick-

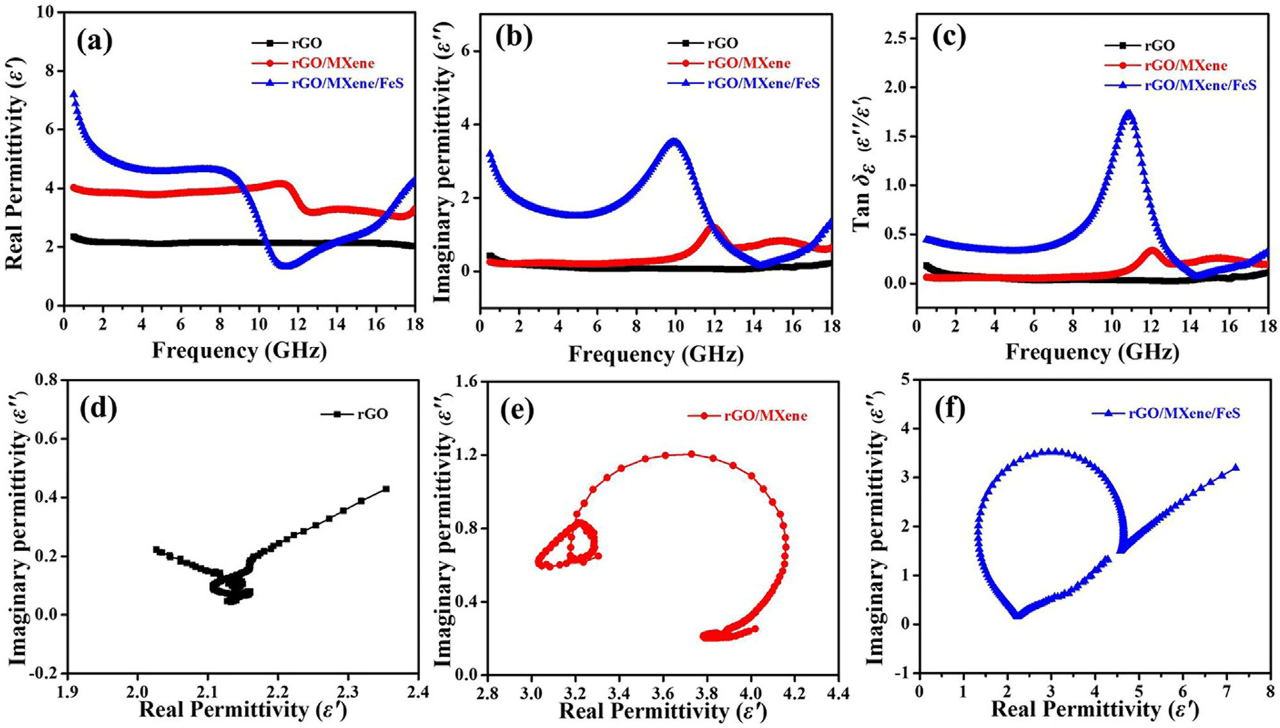

Fig. 3. (a) Real parts and (b) imaginary parts of complex permittivity; (c) dielectric loss tangent of the foams; Cole–Cole curves of (d) rGO, (e) rGO/MXene, and (f) rGO/MXenen/FeS foam.

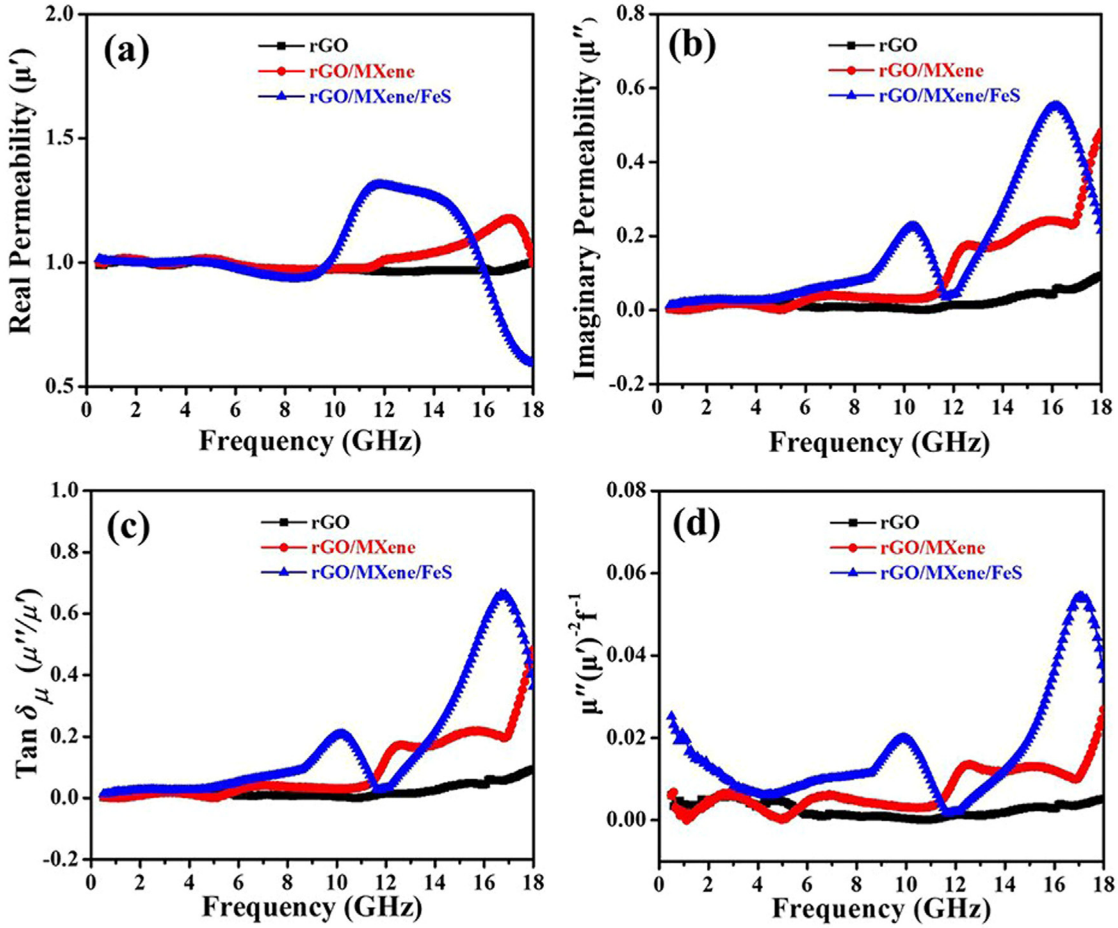

Fig. 4. (a) Real parts and (b) imaginary parts of complex permeability. (c) magnetic loss tangent, and (d) C_0 value of the composite foams.

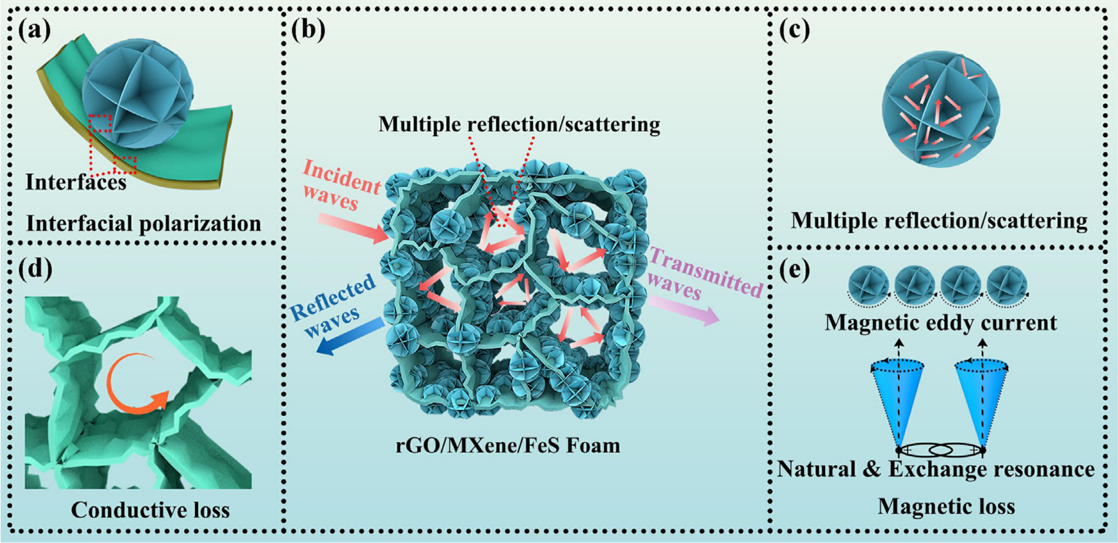

Fig. 5. Microwave absorption mechanisms in rGO/MXene/FeS foam: (a) interfacial polarization; multiple reflection/scattering in (b) foam and (c) FeS clusters; (d) conductive loss; (e) magnetic loss.

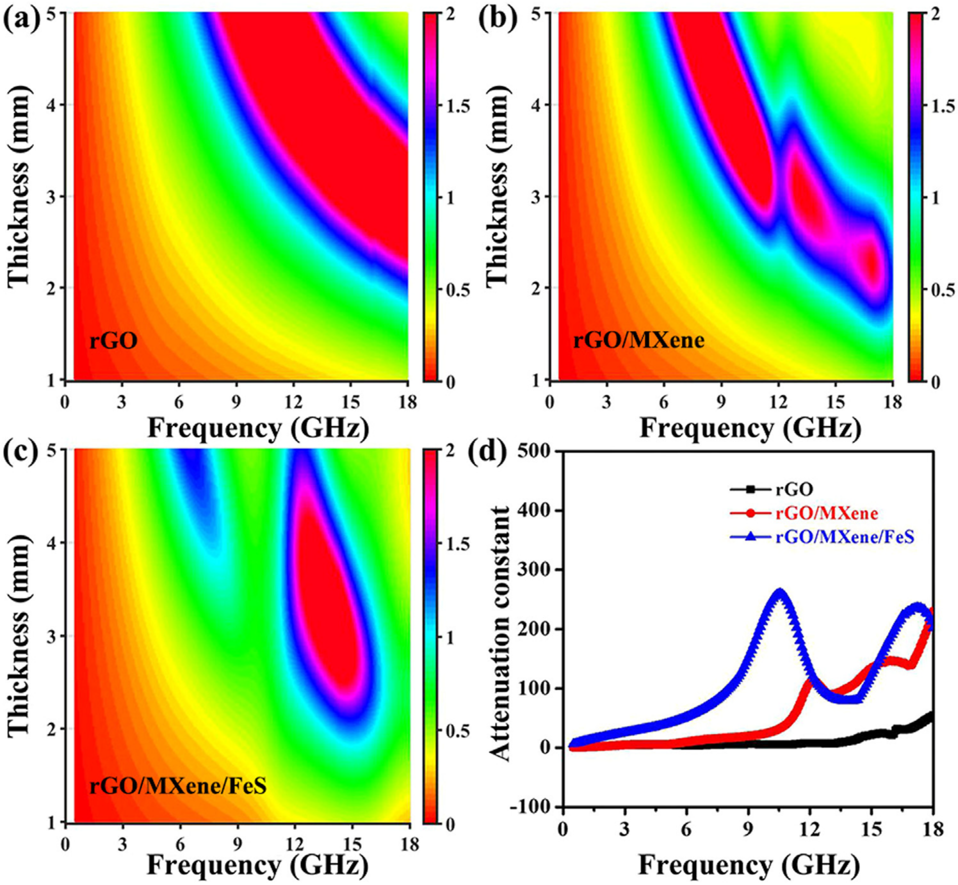

Fig. 6. Impedance matching 2D contour maps ($|Z_{in}/Z_0|$) of (a) rGO, (b) rGO/MXene, and (c) rGO/MXene/FeS, and (d) attenuation constant of the corresponding foams.

ness of the samples; f is the frequency, and c is the light speed at vacuum [44–46]. As a result, the corresponding impedance 2D matching contour maps of those foams are described in Fig. 6(a–c). In the 2D contour maps, the part of sky-blue color indicates that $Z = 1$. Generally, the more the value of Z is close to 1, the better the impedance matching is. Therefore, an excellent impedance matching effect requires that the sky-blue area should be much bigger. As shown in Fig. 6(a, b), after loading of high-conductive MXene, rGO/MXene foam exhibits a poor impedance matching in 2D contour maps, due to the unbridgeable impedance mismatching between MXene coating and air. As a result, most of the incident EMW would be reflected and could not enter the foam. Therefore, it is necessary to introduce a dielectric coating to further optimize the impedance distribution of porous skeletons. In this system, FeS clusters are selected as the dielectric coating and anchored on the surface of MXene coating. As shown in Fig. 6(c), in comparison with rGO and rGO/MXene foam, rGO/MXene/FeS foam exhibits a prominent improvement in the sky-blue area. It suggests a significant optimization of impedance matching performance. Therefore, it can be concluded that the effective construction of the hierarchical impedance gradient structure can accelerate the optimization of impedance matching characteristics in skelectons, leading to more incident EMW entering the foam.

Furthermore, the attenuation constant can be employed to evaluate the attenuation ability for EMW entering the foams, which is quantificationally calculated by Eq. (3):

$$\alpha=\frac{\sqrt{2}\pi f}{c}\sqrt{(\mu''\varepsilon''-\mu'\varepsilon')+\sqrt{(\mu''\varepsilon''-\mu'\varepsilon')^2+(\mu''\varepsilon'+\mu'\varepsilon'')^2}} \tag{3}$$

where ε', ε'', μ', and μ'' are the real and imaginary parts of complex permittivity and permeability, respectively. As displayed in Fig. 6(d), the curves of attenuation constant for those foams show a similar increasing tendency to that of complex permittivity and permeability. rGO/MXene/FeS displays the highest attenuation constant than that of pure rGO and rGO/MXene foam. It indicates that the incident EMW can be dissipated as much as possible. For the composite foams, the gradually enhanced attenuation ability may be also due to the rational construction of magnetic composite foam with a hierarchical impedance structure. As a result, those incident EMWs entering the foam can be efficiently consumed as intrinsic conductive/dielectric loss and magnetic loss as mentioned above. Besides, the effective loading of flower-shaped FeS clusters can increase the magnetic loss of foams as well as other magnetic materials. The difference is that the special flower-shaped structure provides a large number of reflection/scattering sites for incident EMW. Based on the special configuration, multiple reflection/scattering would repeatedly occur between the internal surfaces of foam as demonstrated in Fig. 5(b) and/or arise in the flower-shaped FeS clusters as illustrated in Fig. 5(c). Finally, the dissipation path of EMW can be further prolonged, thereby improving the attenuation constant of the foams.

3.3. Microwave absorption properties of composite foams

The reflection loss (RL) of the incident EMW is an important measure of microwave absorption performance, which can be calculated by transmission line theory [47–50]. Eq. (4) is as follows:

$$\mathrm{RL(dB)}=20\lg\left|\frac{Z_{\mathrm{in}}-Z_0}{Z_{\mathrm{in}}+Z_0}\right| \tag{4}$$

where Z_{in} and Z_0 represent the normalized input impedance of absorbers and the impedance of free space, respectively. Fig. 7 shows 3D reflection loss and the corresponding 2D contour and 2D reflection loss maps of the foams. Moreover, they are also summarized in Table S1 (listed in Supporting Information). As displayed in Fig. 7, rGO/MXene/FeS shows a higher MA performance than that of rGO and rGO/MXene foams. The $\mathrm{RL_{min}}$ value of rGO is only −4.93 dB (Fig. 7(a, d, g)). After loading of MXene nanosheets, the composite foam shows an obvious improvement in MA performance as described in Fig. 7(b, e, h). The $\mathrm{RL_{min}}$ value of rGO/MXene reaches −19.89 dB. And the corresponding EAB is 0.68 GHz (17.32–18 GHz). The positive evolution may be attributed to the formation of a higher conductive-loss network and interfacial polarization between MXene coating and rGO skeletons as demonstrated in Fig. 3. However, further improvement is severely hindered due to the undesired surface impedance mismatching of MXene coating for incident EMW entering the foam. After being incorporated with flower-shaped FeS clusters, rGO/MXene/FeS foam exhibits more outstanding MA performance than rGO/MXene. As shown in Fig. 7(c, f, i), $\mathrm{RL_{min}}$ of the foam reaches a lower value of −47.17 dB as the thickness and frequency are set at 4.78 mm and 7.85 GHz. Meanwhile, the corresponding EAB of rGO/MXene/FeS foam can be further extended to 6.15 GHz (from 6.41 to 12.56 GHz), involving C, X, and Ku bands. What's more, the maximum value of EAB can be up to 6.39 GHz (6.45–12.84 GHz). The significant enhancement in electromagnetic absorption capacity and bandwidth can be easily ascribed to the synergistic effect of optimal impedance matching and improved attenuation characteristics as discussed in Fig. 6. As a result, more incident EMW can enter the materials and thus dissipate as much as possible after entering the foam, endowing the foam with an excellent electromagnetic absorption capacity. Meanwhile, the formation of hierarchical impedance structure in the porous skeletons can prominently broaden the effective absorption bandwidth of foams. Those results once again confirm the effectiveness of magnetic FeS clusters on the improvement in MA performance.

Based on the same hierarchical configuration, the optimization of impedance distribution and attenuation characteristic of foams can become a promising route for realizing the controllable adjustment of MA performance. As displayed in Fig. S2, those electromagnetic parameters can be adjusted by controlling the loading concentration of MXene. In Fig. S2(a), the real part of permittivity for the foams tends to increase due to the loading of more conductive coating in the skeletons. At the same time, the resonance peaks of the imaginary part (Fig. S2(b)) and dielectric loss tangent (Fig. S2(c)) arise and shift to high-frequency. Combined with Cole-Cole curves in Fig. S2(d), those evolutions can be attributed to the formation of a higher conductive network and more interfacial polarization between rGO/MXene and MXene/FeS. As to the magnetic parameters, the complex permeability, and magnetic loss tangent display a similar increasing tendency as the loading concentration of MXene increases from 10 to 40 mg/mL in Fig. S2(e–g). The phenomenon may be due to that loading of FeS hybrids is tightly associated with MXene coating. With the increasing MXene concentration, the loading capacity of FeS is improved to a high value, thereby leading to the increase of magnetic parameters. It is worthy to note that the resonance peak of the foams gradually shifts to the low frequency as displayed in Fig. S2(e, g). It may be also attributed to the increased loading capacity of FeS in the system. Based on those electromagnetic parameters, the corresponding impedance matching and attenuation constant are also calculated and displayed in Fig. S2(h–l). It can be clearly seen that the impedance matching is effectively optimized and the attenuation constant is improved to a higher value. The results indicate that the MA performance of those foams shows significant diversity. As shown in Fig. 8 and Table S2, the $\mathrm{RL_{min}}$ value of the foams continuously decrease from −7.53 dB (rGMF-10) to −10.43 dB (rGMF-20), −47.17 (rGMF-30), and then to −60.45 dB (rGMF-40), whereas the corresponding EAB increases from 0 to 1.14 GHz, 6.15 GHz, and 7.37 GHz. Those results once again confirm the effectiveness of MXene content on the controllable adjustment of MA performance.

Besides, the impedance matching and attenuation characteristic of composite foam can be further optimized by controlling the thermal treatment at a low-temperature range, thereby improving the final MA performance. As displayed in Fig. S3, the complex permittivity of those foams displays prominent enhancement with the increasing annealing temperature, whereas the complex permeability of those foams exhibits a slight fluctuation. It may be mainly ascribed to the further thermal reduction of rGO skeletons. For rGO/MXene/FeS (GMF-0), the rGO skeleton is fabricated into the hierarchical foam as a mechanical supporting material, which is only treated at a mild hydrothermal process. Due to the low reduction degree of rGO skeleton, the high impedance characteristic

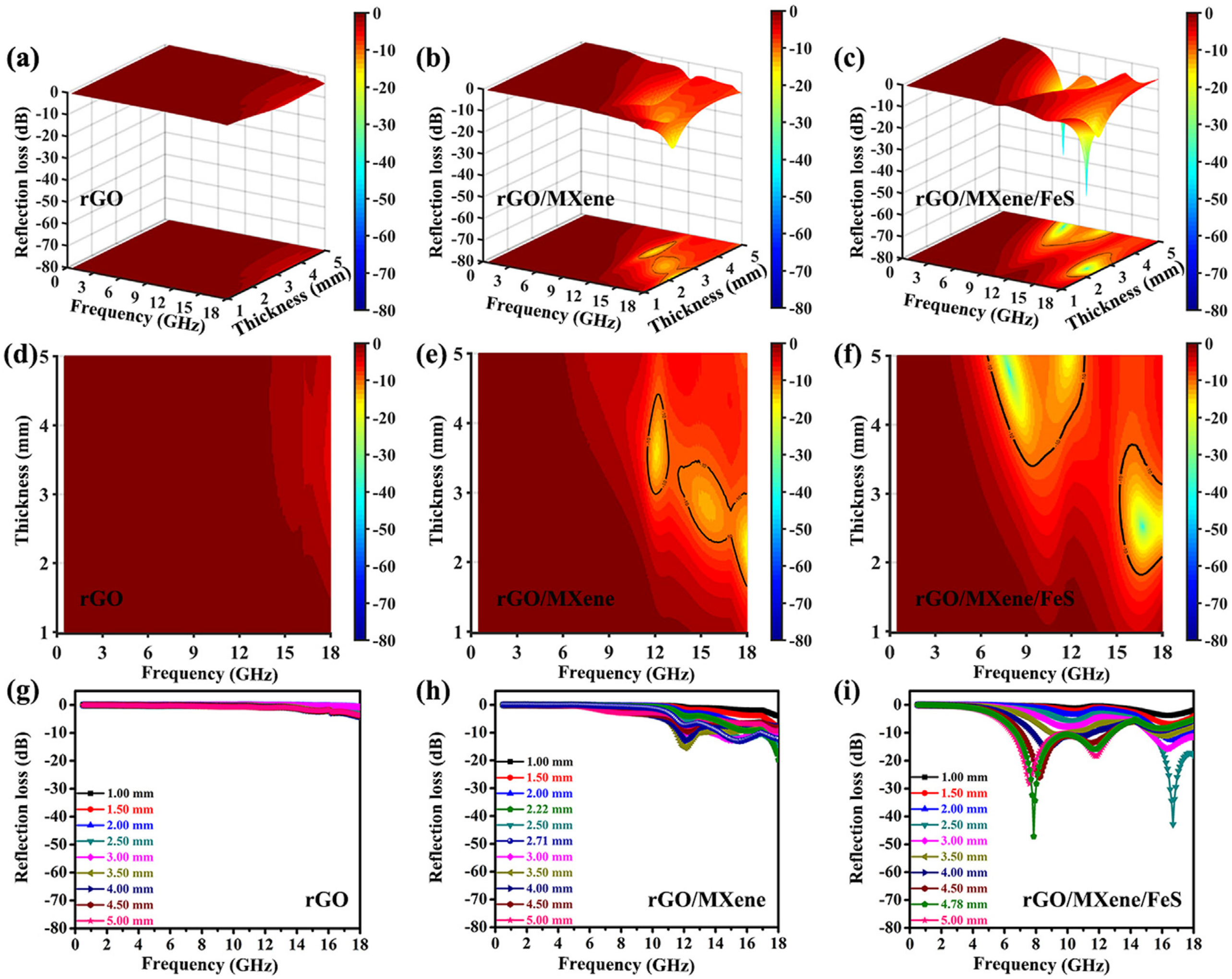

Fig. 7. 3D reflection loss, the corresponding 2D contour and 2D reflection loss maps of the foams: (a, d, g) rGO; (b, e, h) rGO/MXene; (c, f, i) rGO/MXene/FeS.

of the porous network severely restricts the energy consumption of incident EMW as conductive loss. Therefore, an extra thermal treatment can be employed to improve the hierarchical impedance distribution and attenuation characteristic of GMF-0. As a consequence, the impedance matching and attenuation constant of the composite foam are also estimated and recorded in Fig. S3(h–l). The impedance matching of the foams shows an obvious tendency to first increase (from GMF-0 to GMF-200), and then decline (GMF-300), and finally stagnate (GMF-400). Meanwhile, the attenuation constant displays a similar tendency to increase (from GMF-0 to GMF-300) and then decrease (GMF-400) at a high-frequency range of 8–18 GHz. The increase of attenuation constant exhibits a hysteretic behavior in comparison with that of the corresponding impedance matching. Under the synergistic effect of impedance matching and attenuation constant, the final MA performance of the composite foam displays distinct diversity with the increasing annealing temperature. As displayed in Fig. 9 and Table S3, the RL_{min} value of GN/MXene/FeS decreases from –47.17 to –57.06 dB, and then increases to –50.68 and –47.35 dB, maintaining a comparable level. The minimum of RL_{min} arises as the annealing temperature is 200 °C. Meanwhile, the corresponding EAB value displays a gradual increase from 6.15 to 7.56 GHz, 9.66 GHz, and a decrease to 2.55 GHz. The maximum of EAB appears as the annealing temperature is 300 °C. More importantly, the maximum EAB for GMF-300 achieves an unprecedented value of 11.20 GHz (covering 6.10-17.30 GHz), while most traditional materials have difficulty in reaching this level [51–56]. The results confirm the effectiveness of annealing treatment on the adjustment of MA performance. The desynchrony in optimal value between RL_{min} and EAB can be ascribed to the hysteretic behavior of impedance matching and attenuation characteristics as mentioned above. Therefore, it can be concluded that a suitable impedance matching will play a more important role than the attenuation characteristic in improving the entrance and consumption of more incident EMW as much as possible.

For comparison, Table 1 summarizes some recently reported works on porous materials [23,57–67]. As displayed in Table 1, the present foam with ultralight density shows a much larger absorption bandwidth and comparable absorption capacity. For example, $Co_{1.29}Ni_{1.71}O_4$/reduced graphene oxide/calcined melamine ($Co_{1.29}Ni_{1.71}O_4$/rGO/CF) composite foam with a low density of 16.3 mg/cm^3 is designed and successfully constructed via a convenient foaming and calcination method [60]. The RL_{min} value reaches –53.45 dB at the thickness of 3.00 mm, and the corresponding EAB is up to 7.45 GHz. In this work, the RL_{min} of GMF-300 achieves a comparable value of –50.68 dB. Meanwhile, the maximum of EAB can be expanded to 11.20 GHz, which is much wider than the others. It once again confirms the significant effect of hierarchical impedance architectures on the microwave absorption performance. As a consequence, thus excellent broadband MA performance combined with ultralight density makes it possible for the foam to become a promising electromagnetic absorb-

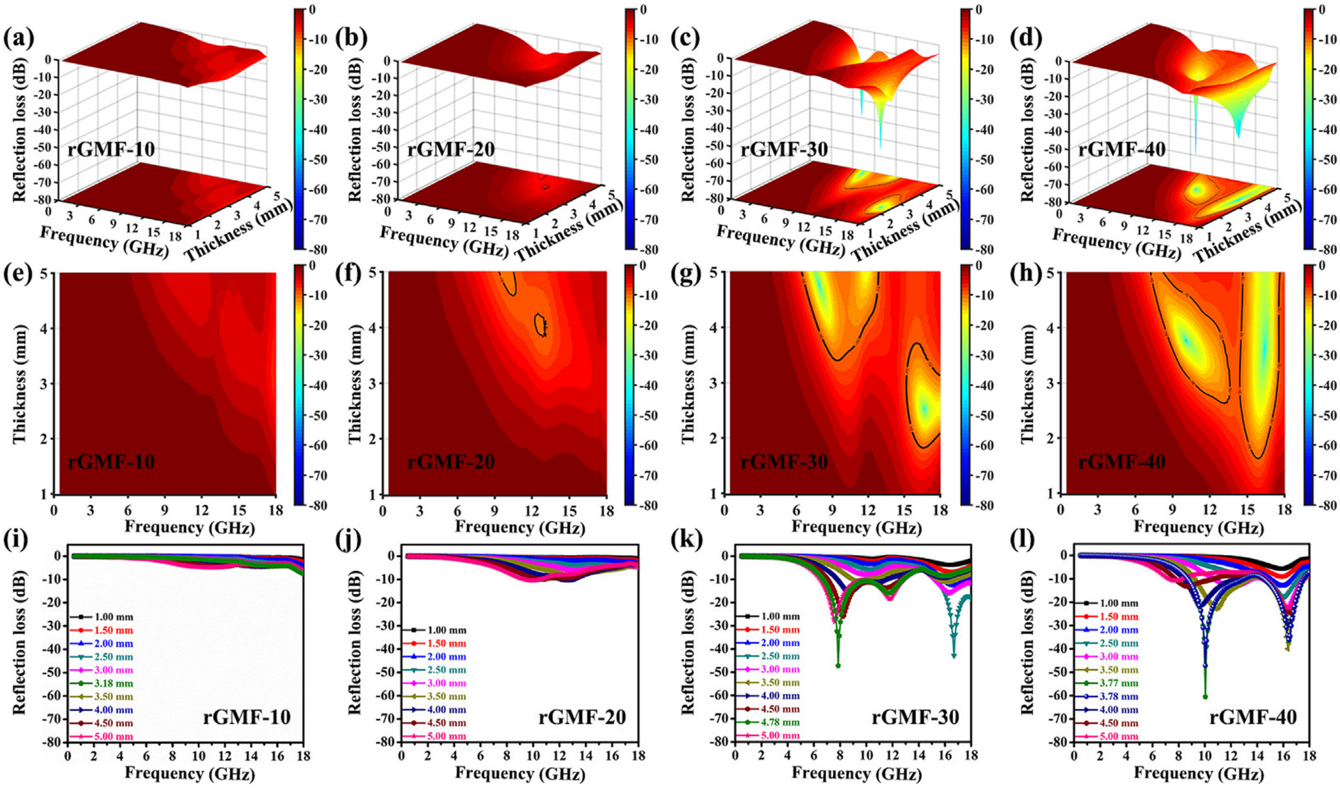

Fig. 8. 3D reflection loss, corresponding 2D contour, and 2D reflection loss maps of the foams: (a, e, i) rGMF-10; (b, f, j) rGMF-20; (c, g, k) rGMF-30; (d, h, l) rGMF-40.

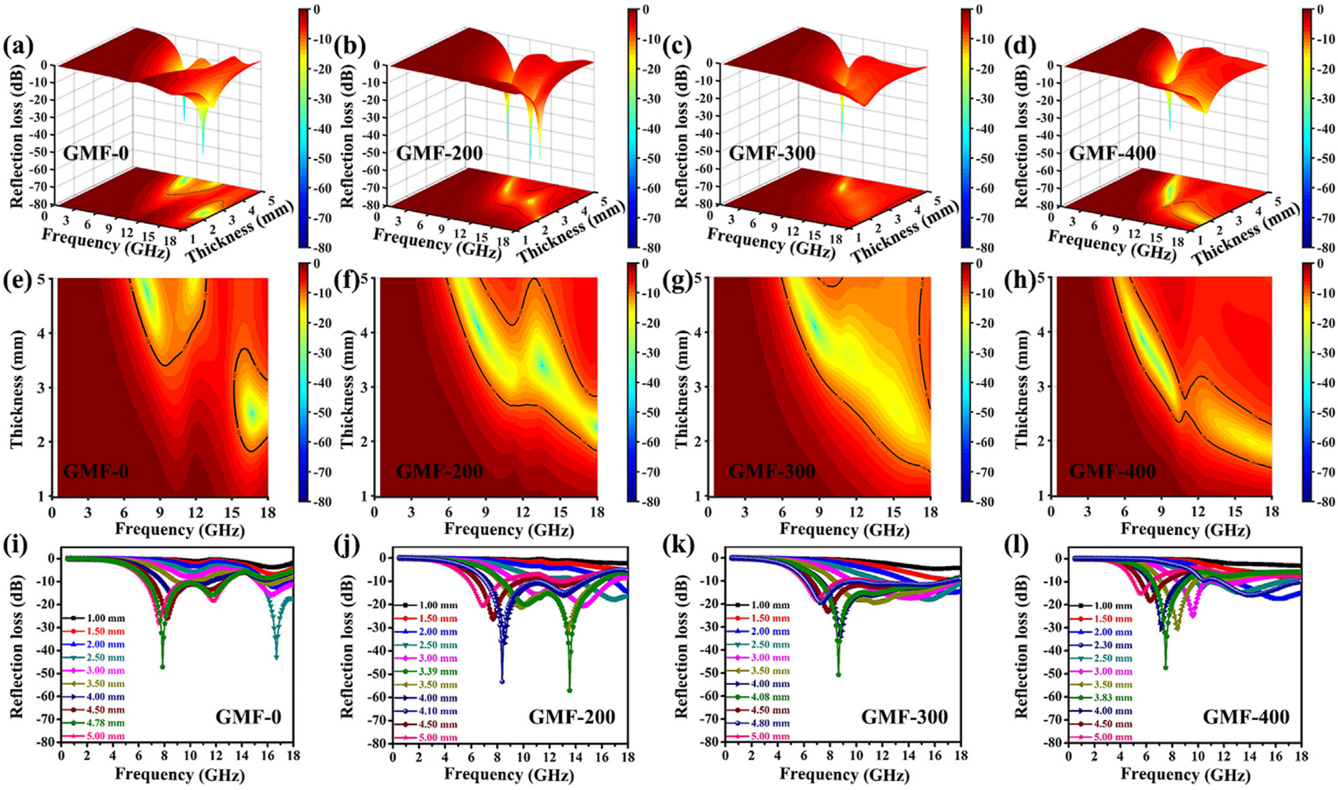

Fig. 9. 3D reflection loss, the corresponding 2D contour and 2D reflection loss maps of the foams: (a, e, i) GMF-0; (b, f, j) GMF-200; (c, g, k) GMF-300; (d, h, l) GMF-400.

Table 1
MA performance of the porous materials reported recently.

	Density (mg/cm^3)	RL$_{min}$ (dB)	Thickness (mm)	Range (GHz)	EAB (GHz)	EAB$_{max}$ (GHz)	Refs.
PI-GP$_{1/3}$-rGO	63.7	−32.90	4.00	8.26–14.48	6.22	6.22	[23]
GF/PA	3.8	−36.50	6.00	6.0–12.0	6.00	8.42	[57]
NRGO/NiFe$_2$O$_4$	10	−60.60	1.50	13.40–18.00	4.60	5.50	[58]
MXene/polyimide	12	−41.80	4.00	14.50–18.00	3.50	6.50	[59]
Co$_{1.29}$Ni$_{1.71}$O$_4$/rGO/CF	16.3	−53.45	3.00	10.55–18.00	7.45	7.45	[60]
MXene/cellulose	310	−43.40	2.00	9.50–14.00	4.50	5.15	[61]
MX/CF/Epoxy	10–20	−41.46	1.83	10.58–15.25	4.67	4.67	[62]
Porous graphene	40–50	−42.9	4.00	5.80–7.30	1.50	5.59	[63]
Ni/carbon	100	−45.00	2.00	11.40–16.00	4.60	4.60	[64]
rGO/MoS$_2$	8.4	−62.92	2.27	9.0–13.4	4.40	4.48	[65]
FeNi@graphene	13.1	−39.39	2.0	11.4–15.8	4.40	8.40	[66]
graphene@SiC	72	−47.3	3	8.5–13.2	4.70	5.40	[67]
rGO/MXene/FeS	12.1	−47.17	4.78	6.41–12.56	6.15	6.39	This work
rGMF-300	11.9	−50.68	4.08	6.91–16.57	9.66	11.20	This work

ing material with a distinct competitive advantage to be applied in aerospace fields.

4. Conclusion

In summary, a novel ultralight magnetic composite foam was prepared by electrostatic self-assembly of MXene on the surface of rGO skeletons, and subsequent hydrothermal anchoring of flower-shaped FeS clusters. The loading of MXene coating increasing conductive loss and FeS clusters improving magnetic loss on the surface of rGO skeletons promotes the formation of hierarchical impedance structure in foams. The rational construction of a hierarchical impedance structure can effectively accelerate the entry of more incident EMW. Under the synergistic effects of various magnetic loss, interfacial polarization, conductive loss, and multiple reflections/scattering, the formation of the hierarchical impedance structure further enhances the attenuation characteristic for EMW entering the foam. As a consequence, the optimal RL$_{min}$ of rGO/MXene/FeS foam with an ultralight density of 12.1 mg/cm^3 reaches −47.17 dB at the thickness of 4.78 mm, and the corresponding EAB is up to 6.15 GHz. More importantly, the adjustment in the loading of MXene and thermal treatment at a low temperature can become an effective means to realize the optimization of whole impedance distribution, endowing the composite foam with an excellent absorption capacity and bandwidth. It is worthy to note that the RL$_{min}$ of GMF-300 achieves a comparable value of −50.68 dB, while the maximum of EAB for GMF-300 can be extended to an unprecedented value of 11.20 GHz (covering 6.10–17.30 GHz). Such excellent MA performance makes it promising to become an efficient electromagnetic absorption material with a distinct competitive advantage.

Acknowledgments

This work was financially supported by the National Natural Science Foundation of China (Nos. 52003106, 21674019), the Fundamental Research Funds for the Central Universities (Nos. JUSRP12032, 2232019A3-03), the China Postdoctoral Science Foundation (No. 2021M691265), the Ministry of Education of the People's Republic of China (No. 6141A0202202), and the Postgraduate Research & Practice Innovation Program of Jiangsu Province (Nos. KYCX22_2319, SJCX22_1110).

Supplementary materials

Supplementary material associated with this article can be found, in the online version, at doi:10.1016/j.jmst.2022.06.018.

References

[1] J.J. Zhang, Z.H. Li, X.S. Qi, X. Gong, R. Xie, C.Y. Deng, W. Zhong, Y.W. Du, Compos. Part B-Eng. 222 (2021) 109067.
[2] L.F. Lyu, F.L. Wang, X. Zhang, J. Qiao, C. Liu, J.R. Liu, Carbon 172 (2021) 488–496.
[3] Y. Wang, X.C. Di, Z. Lu, R.R. Cheng, X.M. Wu, P.H. Gao, Carbon 187 (2022) 404–414.
[4] Q.L. Sun, L. Sun, Y.Y. Cai, W. Ye, S.J. Xu, T. Ji, G.Q. Yuan, Ceram. Int. 45 (2019) 18298–18305.
[5] T.Q. Hou, Z.R. Jia, S.Q. He, Y. Su, X.D. Zhang, B.H. Xu, X.H. Liu, G.L. Wu, J. Colloid Interface Sci. 583 (2021) 321–330.
[6] X.T. Yang, S.G. Fan, Y. Li, Y.Q. Guo, K.P. Ruan, Y.G. Li, S.M. Zhang, J.L. Zhang, J. Kong, J.W. Gu, Compos. Part A Appl. Sci. Manuf. 128 (2020) 105670.
[7] N.N. Wu, B.B. Zhao, J.Y. Liu, Y.L. Li, Y.B. Chen, L. Chen, M. Wang, Z.H. Guo, Adv. Compos. Hybrid Mater. 4 (2021) 707–715.
[8] X.C. Di, Y. Wang, Z. Lu, R.R. Cheng, L.Q. Yang, X.M. Wu, Carbon 179 (2021) 566–578.
[9] Y. Hou, L.F. Cheng, Y.N. Zhang, X.Q. Du, Y.J. Zhao, Z.H. Yang, Chem. Eng. J. 404 (2021) 126521.
[10] Y.X. Zuo, X.X. Su, X.W. Li, Z.J. Yao, T.T. Yu, J.T. Zhou, J. Li, J. Lu, J. Ding, Carbon 167 (2020) 62–74.
[11] R.R. Cheng, Y. Wang, X.C. Di, Z. Lu, P. Wang, M.L. Ma, J.R. Ye, J. Colloid Interface Sci. 609 (2022) 224–234.
[12] X. Fan, F.C. Wang, Q. Gao, Y. Zhang, F. Huang, R.L. Xiao, J.B. Qin, H. Zhang, X.T. Shi, G.C. Zhang, J. Mater. Sci. Technol. 103 (2022) 177–185.
[13] Z.C. Wang, R.B. Wei, J.W. Gu, H. Liu, C.T. Liu, C.J. Luo, J. Kong, Q. Shao, N. Wang, Z.H. Guo, X.B. Liu, Carbon 139 (2018) 1126–1135.
[14] P. Song, B. Liu, C.B. Liang, K.P. Ruan, H. Qiu, Z.L. Ma, Y.Q. Guo, J.W. Gu, Nano Micro Lett. 13 (2021) 91.
[15] Z.C. Wang, R.B. Wei, X.B. Liu, ACS Appl. Mater. Interfaces 9 (2017) 22408–22419.
[16] D.W. Xu, S. Yang, P. Chen, Q. Yu, X.H. Xiong, J. Wang, Carbon 146 (2019) 301–312.
[17] J.M. Tang, N. Liang, L. Wang, J. Li, G. Tian, D. Zhang, S.H. Feng, H.J. Yue, Carbon 152 (2019) 575–586.
[18] S.S. Li, X.W. Tang, Y.W. Zhang, Q.Q. Lan, Z.W. Hu, L. Li, N. Zhang, P.M. Ma, W.F. Dong, W.W. Tjiu, Z.C. Wang, T.X. Liu, ACS Appl. Mater. Interfaces 14 (2022) 8297–8310.
[19] W.W. Gao, N.F. Zhao, T. Yu, J.B. Xi, A.R. Mao, M.Q. Yuan, H. Bai, C. Gao, Carbon 157 (2020) 570–577.
[20] H.L. Lv, Y. Li, Z.R. Jia, L.J. Wang, X.Q. Guo, B. Zhao, R. Zhang, Compos. Part B-Eng. 196 (2020) 108122.
[21] B.H. Yuan, H.J. Tao, S.S. Wang, G.Q. Chen, Y.Y. Zhan, Y. Wang, J.J. Zhou, Compos. Commun. 27 (2021) 100858.
[22] Y. Wang, X. Gao, Y.Q. Fu, X.M. Wu, Q.G. Wang, W.Z. Zhang, C.Y. Luo, Compos. Part B-Eng. 169 (2019) 221–228.
[23] L. Pu, S.S. Li, Y.W. Zhang, H.Y. Zhu, W. Fan, P.M. Ma, W.F. Dong, Z.C. Wang, T.X. Liu, J. Mater. Chem. C 9 (2021) 2086–2094.
[24] J.Q. Wang, L. Liu, S.L. Jiao, K.J. Ma, J. Lv, J.J. Yang, Adv. Funct. Mater. 30 (2020) 2002595.
[25] G. Fang, C.Y. Liu, Y. Yang, K.S. Peng, Y.F. Cao, T. Jiang, Y.T. Zhang, Y. Zhang, ACS Appl. Mater. Interfaces 13 (2021) 37507–37516.
[26] L.Y. Liang, Q.M. Li, X. Yan, Y.Z. Feng, Y.M. Wang, H.B. Zhang, X.P. Zhou, C.T. Liu, C.Y. Shen, X.L. Xie, ACS Nano 15 (2021) 6622–6632.
[27] J.R. Ma, X.X. Wang, W.Q. Cao, C. Han, H.J. Yang, J. Yuan, M.S. Cao, Chem. Eng. J. 339 (2018) 487–498.
[28] S. Huang, L. Wang, Y.C. Li, C.B. Liang, J.L. Zhang, J. Appl. Polym. Sci. 138 (2021) 50649.
[29] Y. Zhang, G.C. Zhang, X.T. Shi, Q. Gao, F. Huang, R.L. Xiao, Compos. Commun. 28 (2021) 100954.
[30] Y.Q. Ma, H.W. Huang, H. Zhou, M. Graham, J. Smith, X.X. Sheng, Y. Chen, L. Zhang, X.Y. Zhang, E. Shchukina, D. Shchukin, J. Mater. Sci. Technol. 95 (2021) 95–104.

[31] J.H. Li, J.Y. Li, H. Meng, S.Y. Xie, B.W. Zhang, L.F. Li, H.J. Ma, J.Y. Zhang, M. Yu, J. Mater. Chem. A 2 (2014) 2934–2941.
[32] J.Z. Zhang, N. Kong, S. Uzun, A. Levitt, S. Seyedin, P.A. Lynch, S. Qin, M.K. Han, W.R. Yang, J.Q. Liu, X.G. Wang, Y. Gogotsi, J.M. Razal, Adv. Mater. 32 (2020) 2001093.
[33] Z.L. Ma, S.L. Kang, J.Z. Ma, L. Shao, Y.L. Zhang, C. Liu, A.J. Wei, X.L. Xiang, L.F. Wei, J.W. Gu, ACS Nano 14 (2020) 8368–8382.
[34] S.W. Cao, Y.J. Zhu, J. Phys. Chem. C 112 (2008) 12149–12156.
[35] F. Cao, W. Hu, L. Zhou, W.D. Shi, S.Y. Song, Y.Q. Lei, S. Wang, H.J. Zhang, Dalton Trans. (2009) 9246–9252.
[36] L.D. Shi, D.Z. Li, J.L. Yu, H.C. Liu, Y. Zhao, H.L. Xin, Y.M. Lin, C.D. Lin, C.H. Li, C.Z. Zhu, J. Mater. Chem. A 6 (2018) 7967–7976.
[37] T.T. Le, X. Liu, P.J. Xin, Q. Wang, C.Y. Gao, Y. Wu, Y. Jiang, Z.J. Hu, S.S. Huang, Z.W. Chen, J. Mater. Sci. Technol. 74 (2021) 168–175.
[38] A. Iqbal, F. Shahzad, K. Hantanasirisakul, M.K. Kim, Y. Gogotsi, C.M. Koo, Science 369 (2020) 446–450.
[39] Z.Y. Jiang, H.X. Si, X. Chen, H.M. Liu, L. Zhang, Y.H. Zhang, C.H. Gong, J.W. Zhang, Compos. Commun. 22 (2020) 100503.
[40] C.H. Sun, Z.R. Jia, S. Xu, D.Q. Hu, C.H. Zhang, G.L. Wu, J. Mater. Sci. Technol. 113 (2022) 128–137.
[41] E.B. Cui, F. Pan, Z. Xiang, Z.C. Liu, L.Z. Yu, J. Xiong, X. Li, W. Lu, Adv. Eng. Mater. 23 (2021) 2000827.
[42] G.H. Cheng, F. Pan, X.J. Zhu, Y.Y. Dong, L. Cai, W. Lu, Compos. Commun. 27 (2021) 100867.
[43] Q. Li, X.J. Tian, W. Yang, L.Q. Hou, Y. Li, B. Jiang, X. Wang, Y.F. Li, Appl. Surf. Sci. 530 (2020) 147298.
[44] Y.X. Li, Y.J. Liao, L.Z. Ji, C.L. Hu, Z.H. Zhang, Z.Y. Zhang, R.Z. Zhao, H.W. Rong, G.W. Qin, X.F. Zhang, Small 18 (2022) 2107265.
[45] J.J. Pan, X. Sun, T. Wang, Z.T. Zhu, Y.P. He, W. Xia, J.P. He, Appl. Surf. Sci. 457 (2018) 271–279.
[46] D. Lan, Z.G. Gao, Z.H. Zhao, K.C. Kou, H.J. Wu, Compos. Commun. 26 (2021) 100767.
[47] Y.L. Zhang, Z.L. Ma, K.P. Ruan, J.W. Gu, Nano Res. 15 (2022) 5601–5609.
[48] P.B. Liu, S. Gao, G.Z. Zhang, Y. Huang, W.B. You, R.C. Che, Adv. Funct. Mater. 31 (2021) 2102812.
[49] R.W. Shu, Z.L. Wan, J.B. Zhang, Y. Wu, J.J. Shi, Compos. Sci. Technol. 210 (2021) 108818.
[50] L. Wang, Z.L. Ma, Y.L. Zhang, H. Qiu, K.P. Ruan, J.W. Gu, Carbon Energy 4 (2022) 200–210.
[51] Y.F. Cao, C.Y. Liu, Z.R. Xue, T. Jiang, G. Fang, K.S. Peng, Y.J. Zhang, Ceram. Int. 48 (2022) 5824–5830.
[52] H.X. Xu, G.Z. Zhang, Y. Wang, M.Q. Ning, B. Ouyang, Y. Zhao, Y. Huang, P.B. Liu, Nano Micro Lett. 14 (2022) 102.
[53] K. Su, Y. Wang, K.X. Hu, X. Fang, J. Yao, Q. Li, J. Yang, ACS Appl. Mater. Interfaces 13 (2021) 22017–22030.
[54] Y. Huang, J. Yan, S.H. Zhou, J.Y. Yang, P.B. Liu, J. Mater. Sci. Mater. Electron. 29 (2018) 70–79.
[55] C.Q. Song, X.W. Yin, M.K. Han, X.L. Li, Z.X. Hou, L.T. Zhang, L.F. Cheng, Carbon 116 (2017) 50–58.
[56] K.X. Hu, H.H. Wang, X. Zhang, H. Huang, T. Qiu, Y. Wang, C.F. Zhang, L.M. Pan, J. Yang, Chem. Eng. J. 408 (2021) 127283.
[57] Z. Cheng, R.F. Wang, Y.S. Cao, Z.W. Zhang, W.L. Ma, T.R. Zhang, F. Fan, Y. Huang, ACS Appl. Mater. Interfaces 14 (2022) 3218–3232.
[58] L.L. Deng, R.W. Shu, J.B. Zhang, J. Colloid Interface Sci. 614 (2022) 110–119.
[59] Y. Dai, X. Wu, Z. Liu, H.B. Zhang, Z.Z. Yu, Compos. Part B-Eng. 200 (2020) 108263.
[60] Y.A. Shi, X.Y. Ding, K.C. Pan, Z.H. Gao, J. Du, J. Qiu, J. Mater. Chem. A 10 (2022) 7705–7717.
[61] Y. Jiang, X. Xie, Y. Chen, Y.J. Liu, R. Yang, G.X. Sui, J. Mater. Chem. C 6 (2018) 8679–8687.
[62] T.P. Sun, Z.W. Liu, S. Li, H.S. Liu, F. Chen, K. Wang, Y. Zhao, Compos. Part A-Appl. Sci. Manuf. 150 (2021) 106594.
[63] C. Chen, J.B. Xi, E.Z. Zhou, L. Peng, Z.C Chen, C. Gao, Nano Micro Lett. 10 (2017) 26.
[64] H.B. Zhao, Z.B. Fu, H.B. Chen, M.L. Zhong, C.Y. Wang, ACS Appl. Mater. Interfaces 8 (2016) 1468–1477.
[65] C. Li, Z.H. Li, X.S. Qi, X. Gong, Y.L. Chen, Q. Peng, C.Y. Deng, T. Jing, W. Zhong, J. Colloid Interface Sci. 605 (2022) 13–22.
[66] J. Xu, X. Zhang, H.R. Yuan, S. Zhang, C.L. Zhu, X.T. Zhang, Y.J. Chen, Carbon 159 (2020) 357–365.
[67] Y. Jiang, Y. Chen, Y.J. Liu, G.X. Sui, Chem. Eng. J. 337 (2018) 522–531.